

Solar Corona Loop Studies with AIA: I. Cross-Sectional Temperature Structure

Markus J. Aschwanden and Paul Boerner

*Lockheed Martin Advanced Technology Center, Solar & Astrophysics Laboratory, Org. ADBS, Bldg.252,
3251 Hanover St., Palo Alto, CA 94304, USA; e-mail: aschwanden@lmsal.com*

ABSTRACT

We present a first systematic study on the cross-sectional temperature structure of coronal loops using the six coronal temperature filters of the Atmospheric Imaging Assembly (AIA) instrument on the Solar Dynamics Observatory (SDO). We analyze a sample of 100 loop snapshots measured at 10 different locations and 10 different times in active region NOAA 11089 on 2010 July 24, 21:00-22:00 UT. The cross-sectional flux profiles are measured and a cospatial background is subtracted in 6 filters in a temperature range of $T \approx 0.5 - 16$ MK, and 4 different parameterizations of differential emission measure (DEM) distributions are fitted. We find that the reconstructed DEMs consist predominantly of narrowband peak temperature components with a thermal width of $\sigma_{\log(T)} \leq 0.11 \pm 0.02$, close to the temperature resolution limit of the instrument, consistent with earlier triple-filter analysis from TRACE by Aschwanden and Nightingale (2005) and from EIS/Hinode by Warren et al. (2008) or Tripathi et al. (2009). We find that 66% of the loops could be fitted with a narrowband single-Gaussian DEM model, and 19% with a DEM consisting of two narrowband Gaussians (which mostly result from pairs of intersecting loops along the same line-of-sight). The mostly isothermal loop DEMs allow us also to derive an improved empirical response function of the AIA 94 Å filter, which needs to be boosted by a factor of $q_{94} = 6.7 \pm 1.7$ for temperatures at $\log(T) \lesssim 6.3$. The main result of near-isothermal loop cross-sections is not consistent with the predictions of standard nanoflare scenarios, but can be explained by flare-like heating mechanisms that drive chromospheric evaporation and upflows of heated plasma coherently over loop cross-sections of $w \approx 2 - 4$ Mm.

Subject headings: Sun: corona — Sun: UV radiation — Sun: magnetic topology

1. INTRODUCTION

The plasma dynamics in the solar corona is controlled by the magnetic field, which channels plasma flows along one-dimensional (1-D) fluxtubes due to the low plasma- β parameter that prevails in most parts of the corona. This basic 1-D transport process organizes the solar corona into bundles of fluxtubes along open or closed magnetic field lines, which we generically call “coronal loops” (for an overview, e.g., see Aschwanden 2006). The fine structure and composition of coronal loops, however, is still a subject of debate, which has culminated into two schools of thought. One theory, mostly inspired by Eugene Parker (1988), assumes a highly inhomogeneous loop fine structure consisting of twisted and braided strands that may be produced as a result of microscopic magnetic reconnection events, called nanoflares (e.g., see review by Klimchuk 2006), which predicts a broad temperature distribution of unresolved strands and constitutes a multi-thermal loop. Alternatively, loops are thought to have a homogeneous and near-isothermal cross-section on a resolved spatial scale of $\gtrsim 1$ Mm, if they are filled up by a macroscopic chromospheric evaporation process such as the one known to operate during flares (e.g., review by Antonucci et al. 1999). This theory predicts a narrow temperature distribution, which is referred to as a monolithic or isothermal loop. The determination

of the cross-sectional temperature structure, the prime focus of this paper, is therefore a crucial method to distinguish between these two opposite scenarios of microscopic or macroscopic plasma heating processes in the solar corona.

The cross-sectional temperature structure of coronal loops has been studied early on from EUV and soft X-ray images with Skylab, Yohkoh, SMM, SoHO/EIT, and CDS, but the spatial resolution of these instruments was limited to a range of $\approx 2.5'' - 10''$ ($\approx 2 - 7$ Mm). This is a typical spatial scale of multi-thermal loop bundles that consist of ensembles of many unresolved loop strands, which are resolved when inspected with high-resolution images, such as with TRACE with a pixel size of $0.5''$ (corresponding to an effective spatial resolution of $\approx 1.25''$, i.e., ≈ 0.9 Mm; Gburek et al. 2006). Analysis of high-resolution TRACE images with three temperature filters in the range of $T \approx 0.7 - 2.7$ MK has given support for near-isothermal loops (Del Zanna and Mason 2003; Aschwanden and Nightingale 2005; Warren et al. 2008, or Tripathi et al. 2009, using also Hinode/EIS data), but multi-thermality in loops have also been claimed (Schmelz et al. 2009). Each applied method has been criticized for different reasons: (i) Loop-associated fluxes can be heavily contaminated by the multi-thermal background of other loops along a line-of-sight if the background is not measured cospatially to the target loop, which unavoidably leads to a multi-thermal bias; (ii) triple-filter analysis has a limited temperature range and thus may not reveal the full temperature width of a differential emission measure (DEM) distribution, leading to an isothermal bias; or (iii) the inversion of a DEM from triple-filter data is underconstrained and biased towards the temperature range with the highest instrumental sensitivity. All three problems can now be significantly mitigated with data from the new *Atmospheric Imaging Assembly (AIA)* (Lemen et al. 2011; Boerner et al. 2011) onboard the *Solar Dynamics Observatory (SDO)*, which observes the Sun with 8 different temperature filters, with an uninterrupted cadence of 12 s, and a pixel size of $0.6''$ (corresponding to a spatial resolution of $\approx 1.6''$ or ≈ 1.2 Mm; Boerner et al. 2001).

In this Paper we present a multi-temperature analysis of 100 loop segments observed at 10 different spatial locations and 10 different times. Section 2 contains the description of the data analysis and results in terms of differential emission measure (DEM) distribution modeling, while Section 3 contains a discussion of the results and theoretical consequences, followed by conclusions in Section 4.

2. DATA ANALYSIS

2.1. Instrument

AIA saw first light on 2010 March 29 and produced since then continuous data of the full Sun with a 4096×4096 detector with a pixel size of $0.6''$, corresponding to an effective spatial resolution of $\approx 1.6''$. AIA contains 10 different wavelength channels, three in white light and UV, and seven EUV channels, whereof six are centered on strong iron lines, covering the coronal range from $T \approx 0.6$ MK to $\gtrsim 16$ MK. AIA records a set of 8 near-simultaneous images in each filter every 12 s. The number of temperature channels was chosen to be compatible with the achievable temperature resolution, which is approximately a Gaussian half width of $\sigma_{\Delta \log(T_e)} \approx 0.1$ (corresponding to a full width of half peak of $\Delta \log(T_e) \approx 0.25$). The lines were chosen to be emitted by ions of a single element, i.e., iron, to avoid a dependence on the relative abundances in the coronal plasma. A list of the AIA temperature channels is given in Table 1. The contributions of different coronal regions (coronal holes, quiet Sun, active regions, flare plasma) to the different AIA EUV channels was studied in Boerner et al. (2001) and O’Dwyer et al. (2010), predicting count rates of $10^1 - 10^5$ DN s^{-1} for the 6 coronal AIA channels. The temperature resolution is fundamentally limited due to systematic

errors in atomic excitation calculations and data noise (Judge 2010).

2.2. Observations and Loop Selection

For the analysis of individual coronal loops we prefer an active region near disk center, because the line-of-sight or column depth is smallest at disk center, and thus contains the least confusion by secondary loops. A suitable active region is NOAA AR 11089, which crossed the central meridian on 2010 July 24, which we have chosen for analysis here. In each of the 6 coronal filters we analyze 10 loops at 10 different times (i.e., 100 events), in time steps of approximately 6 min, equally spaced during the time interval of 21:00-22:00 UT.

The 100 loop events have 10 different positions, with locations spread all over the active region AR 11089. We selected loops with a good signal-to-noise ratio, which are mapped out in Fig. 1. The partial image shown in Fig. 1 (and all other analyzed images) have a center position located at $(-91'', -413'')$ from Sun center and a size of $(720, 800)$ pixels, corresponding to a field-of-view of $(432'', 480'')$. All positional information of the displayed images (Figs. 1 and 2) and loop coordinates are given in units of the pixel values $(0 < x < 720, 0 < y < 800)$ of the partial images, which can be downloaded in this format from the *Solar Software (SSW) service request* archive of AIA.

The selection contains 6 cases of loops detected in 6 different filters at coronal temperatures labeled (after the wavelength channel in which they were identified) as 131a, 171a, 193a, 211a, 335a 94a) and 4 additional cases chosen in the loop-rich 171 Å filter (labeled as 171b, 171c, 171d, 171e). The last case (171e) was deliberately chosen in the same loop structure as the first case (171a), but in a different segment and distance from the loop footpoint. The center coordinates of the selected loop segments are listed in Table 2. The spines of the selected loop segments together with the encompassing boxes that define the location of the background are all shown on the same 171 Å image in Fig. 1, rendered with an inverse greyscale (Fig. 1 top) and with a highpass filter (Fig. 1, bottom). The loop segments have arbitrary lengths in the range of $n_s \approx 20 - 90$ pixels ($\approx 10 - 40$ Mm). Curved data stripes (aligned with the loop spines) with a width of $n_w = 20$ pixels (9 Mm) have been extracted for measurements of the loop width w , cross-sectional flux profiles $F_\lambda(x)$, and background profiles $B_\lambda(x)$. Enlarged subimages (with a size of 100×100 pixels, or 44 Mm^2) of the selected loops and extracted data stripes are shown in Fig. 2, along with highpass-filtered renderings to enhance the loop structures. The enlarged maps show the context of the target loops and neighbored loop structures. Thus, a total of $n = n_L \times n_\lambda \times n_t = 600$ subimages were extracted, for each of the selected loops ($n_L = 10$), for different times ($n_t = 10$), and all six coronal filters ($n_\lambda = 6$).

2.3. Solar Rotation

Since we analyze each loop at 10 different times during a time interval of an hour and the SDO spacecraft has a fixed pointing towards Sun center, we have to take the solar rotation into account, which shifts the loop positions in east-west direction (at the central meridian) by an amount of

$$\Delta x(\Delta t) = \frac{\Delta t}{T_{syn}} \frac{2\pi(R_\odot + h)}{(0.6'' \times 0.725 \text{ Mm}/'')} \cos(b - b_0) \cos(l - l_0) , \quad (1)$$

with the solar radius $R_\odot = 696 \text{ Mm}$, the average altitude of EUV emission $h \lesssim 0.1R_\odot$, the synodic solar rotation period of $T_{syn} = 27.2753 \text{ days}$, the solar latitude of $(b - b_0) \approx 45^\circ$ and longitude $(l - l_0) \approx 0^\circ$ with

respect to Sun center (l_0, b_0) , amounting up to $\Delta x(\Delta t = 1 \text{ hour}) \approx 12$ pixels. The corresponding pixel shifts have to be added to the loop coordinates given in Table 2, with respect to the reference time of 2010 July 24, 21:00 UT.

2.4. Cross-sectional Loop Flux and Background Flux Profiles

For each selected loop we mark the start, midpoint, and end position of the loop spine and interpolate a 2D-spline function with steps of one pixel in order to obtain a smooth curvature. A curved array aligned with the positions $s_j, j = 1, \dots, n_s$ along the loop spine is then computed in perpendicular direction $x_i = 1, \dots, n_w$ at each spine point, yielding the flux values $F_\lambda(x_i, s_j)$ in a cartesian grid that corresponds to the stretched-out loop. The total flux of these stretched-out subimages are shown in Fig. 3 in each of the 6 wavelength filters for the first time interval $t_1 \approx 21:00$ UT of each different loop position. The cross-sectional total flux profiles are then computed by averaging the 2-D fluxes $F_\lambda(x_i, x_j)$ along the loop spine,

$$F_\lambda^{tot}(x_i) = \frac{1}{n_s} \sum_{j=1}^{n_s} F_\lambda^{tot}(x_i, x_j) , \quad (2)$$

where the fluxes are given in units of datanumbers per second (DN s⁻¹) after normalizing the counts (DN) by the exposure time, which is different in each filter. The so-obtained cross-sectional flux profiles $F_\lambda^{tot}(x_i)$ are shown in Fig. 3 (top), which sometimes reveal substantial slopes of the cospatial background.

We characterize the flux profiles with a Gaussian cross-sectional fit $G_\lambda(x_i)$ that includes a sloped background profile,

$$G_\lambda(x) = F_0 \exp\left(-\frac{(x - x_0)^2}{2\sigma_w^2}\right) + B_0 + B_1(x - x_0) . \quad (3)$$

This 5-parameter fit $(F_0, x_0, \sigma_w, B_0, B_1)$ is executed for each of the 600 flux profiles (of which 60 are shown in Fig. 3 top for the first time interval t_1). Secondary loops that occasionally appear at the edge of the analyzed windows are eliminated by apodization of the Gaussian fit outside of the flux minima on both sides of the target loop. This method defines a cospatial linear background profile,

$$B_\lambda(x) = B_0 + B_1(x - x_0) , \quad (4)$$

and is supposed to remove the loop-unrelated EUV flux along the same line-of-sight intersecting with the loop center position. The cospatial definition of the loop and background is crucial for an accurate determination of the loop-associated flux, while any background evaluation at arbitrary locations away from the loop is spoiled by substantial contamination of loop-unrelated flux along the line-of-sight.

The loop centroid positions x_0 were found to vary slightly (in the order of 1-2 pixels) between different temperature filters, which indicates some imperfect knowledge of the pointing offset between different filters, but they do not affect our results here, because the loop-related flux F_0 is evaluated at the loop centroid position x_0 with the Gaussian fit method. The knowledge of the pointing offset between the channels is expected to improve to < 1 pixel.

The full width at half maximum (FWHM) of the loops, w , is related to the Gaussian widths σ_w by,

$$w = 2\sqrt{2 \log 2} \sigma_w \approx 2.35 \sigma_w . \quad (5)$$

We calculated also the cross-correlation coefficients between the 2-D stretched-out images $F_\lambda(x_i, s_j)$ of each wavelength with that of the detection wavelength, which are given in each subimage in Fig. 3. For

instance, the loop 171c has been detected in the wavelength of 171 Å, but shows no recognizable Gaussian cross-section in 335 Å (Fig. 3 top). Thus, the flux in the 335 Å channel is expected to be uncorrelated with the loop detected in 171 Å. The cross-correlation coefficient is indeed very low with $CCC(\lambda_{171}, \lambda_{335}) = 0.193$ (Fig.3). In the calculation of the cross-correlation coefficients we compensated relative offsets between the wavelength filters up to ≤ 3 pixels.

2.5. Method of Differential Emission Measure Distribution Fits

The background-subtracted loop fluxes $F_{0\lambda}$ in each of the 6 coronal wavelength filters are essentially the relevant quantities that constrain the underlying differential emission measure (DEM) distribution $dEM(T)/dT$ of a particular loop cross-section,

$$F_{0\lambda} = \int \frac{dEM(T)}{dT} R_{\lambda}(T) dT = \sum_k EM(T_k) R_{\lambda}(T_k), \quad (6)$$

where $R_{\lambda}(T)$ is the instrumental temperature response function of each filter λ . Since the inversion of the DEM is somewhat under-constrained with a set of 6 flux measurements, we employ a forward-fitting technique with parameterized DEM distribution functions.

We choose 4 different parameterizations of DEM functions, which all consist of superpositions of a variable number of Gaussians as a function of the logarithmic temperature, but all have 6 free parameters: (1) a single-Gaussian (EM_0, T_0, σ_{T0}) with 3 additional fixed Gaussians with amplitudes EM_1, EM_2, EM_3 at fixed temperatures $\log(T_k) = 5.7 + 0.4(k-1)$, $k = 1, \dots, 3$; (2) a double-Gaussian ($EM_0, EM_1, T_0, T_1, \sigma_{T0}, \sigma_{T2}$), (3) a six-Gaussian DEM ($EM_k, k = 1, \dots, 6$ at 6 pre-defined temperatures $\log(T_k) = 5.7 + 0.2(k-1)$, $k = 1, \dots, 6$ with narrow temperature widths $\sigma_T = 0.1$), and (4) the same six-Gaussian DEM function with broad temperature widths $\sigma_T = 0.5$:

$$EM(T) = \sum_{k=1}^n EM_k \exp\left(-\frac{[\log(T) - \log(T_k)]^2}{2\sigma_k^2}\right) \begin{cases} n = 4, \text{ single - Gaussian } (EM_1, T_1, \sigma_1, EM_2, EM_3, EM_4) \\ n = 2, \text{ double - Gaussian } (EM_1, T_1, \sigma_1, EM_2, T_2, \sigma_2) \\ n = 6, \text{ narrow six - Gaussian } (EM_1, \dots, EM_6, \sigma_T = 0.1) \\ n = 6, \text{ broad six - Gaussian } (EM_1, \dots, EM_6, \sigma_T = 0.5) \end{cases} \quad (7)$$

Examples of the four DEM parameterizations are shown in Fig. 4, where a fit of each parameterization to an observed DEM (Brosius et al. 1996) is visualized. The choice of these 4 parameterizations is motivated by the aim to cover the whole range from isothermal to multi-thermal distributions, but with the same number of six free parameters matching the six flux constraints. The first 3 models with 1-6 Gaussians can all mimic near-isothermal DEM distributions, while all 4 models can also represent broadband multi-thermal DEM distributions. Because the average temperature steps between the peak response of the different filters is $\Delta \log(T) \approx 0.2$, we have to limit the Gaussian width in the DEM models to $\sigma_T \gtrsim 0.1$. In addition, in order to avoid under-constrained solutions outside the sensitivity range of the 6 coronal AIA temperature filters we set also limits of $5.7 \leq \log(T) \leq 7.0$.

Our forward-fitting procedure uses a model $F_{\lambda}^{mod}(x)$ than consists of a convolution of the spatial Gaussian loop cross-sectional profile $g(x) = [G_{\lambda}(x) - B_{\lambda}(x)]/F_0$ with the temperature DEM functions $EM(T)$

$$F^{mod}(x, \lambda) = \exp\left(-\frac{(x - x_{0,\lambda})^2}{2\sigma_{w,\lambda}^2}\right) \sum_k EM(T_k) R_{\lambda}(T_k), \quad (8)$$

which is then fitted to the observed cross-section profiles $F^{obs}(x, \lambda)$ (Eq. 2), using the χ^2 -criterion,

$$\chi_{red}^2 = \frac{1}{(n - n_{free})} \sum_{i,j} \frac{(F^{obs}(x_i, \lambda_j) - F^{mod}(x_i, \lambda_j))^2}{\sigma^2(\lambda_j)}, \quad (9)$$

where $n = n_w n_\lambda = 20 \times 6$ is the number of measurements, $n_{free} = 6$ is the number of free variables of the model, and the expectation value of the uncertainty $\sigma(\lambda_j)$ in each wavelength filter is estimated from the mean standard deviations of the Gaussian cross-section profile fits $G_\lambda(x)$ (Eq. 3) to the observed values $F_\lambda(x)$ (Eq. 2) without DEM constraints,

$$\sigma(\lambda_j) = \sqrt{\frac{1}{n_w} \sum_i [G_{\lambda_j}(x_i) - F_{\lambda_j}^{tot}(x_i)]^2}. \quad (10)$$

This χ^2 -criterion yields a value of exactly unity if a perfect solution of the DEM is found that matches each loop flux. In reality we expect some uncertainties in the background subtraction that result into inconsistent flux values that cannot perfectly be fitted by any DEM. Since the expectation values of the uncertainties given in Eq. (10) are empirically determined, it includes all possible deviations from a perfect fit of a Gaussian spatial cross-section, which includes the Poisson noise of photons, small fluctuations due to real loop substructures (e.g., loop strands), or any instrumental effects.

We encoded our forward-fitting procedure using the *Interactive Data Language (IDL)* routine *POWELL*, which is based on Powell’s method of minimization of functions in multi-dimensions (Press et al. 1986). The convergence of the Powell method in multiple dimensions often depends on the accuracy of the initial guess values. For the initial guesses we estimate first the temperature and emission measure of the DEM peak by an inversion of simplified response functions, approximated by a single peak, which yields the approximate diagonal values of the inversion matrix. We test the convergence behavior of our code also by optimization of the linear as well as logarithmic emission measure and find identical convergence values. A test series of the reliability of our DEM inversion method is described in Appendix A.

3. RESULTS

3.1. DEM Fits

In total we fitted 100 loop events with 4 different DEM models, each one simultaneously in 6 filters and 20 spatial positions across the loop cross-section. We show the best-fit solutions of these 100 loop events at the loop centroid position $x = x_0$ with the 2-Gaussian DEM model in Fig. 5. The total flux is generally matched in each filter within a few percents accuracy, although most loops show a significant evolution during the analyzed time interval.

We express the goodness-of-fit with the χ^2 -criterion as defined in Eq. (9) and sample the distributions of their values in form of histograms in Fig. 6, for each of the 4 DEM models separately. All methods are bound by a lower value of $\chi^2 \gtrsim 1$ for the best fits, which is expected according to our definition of expectation values of uncertainties.

If we choose $\chi^2 \leq 2$ as a criterion for acceptable fits, the single-Gaussian DEM model yields 66% acceptable fits, the double-Gaussians DEM model yields 85% acceptable fits, the narrowband six-Gaussian DEM yields 50%, and the broadband six-Gaussian DEM model only 20%, while 14% of the cases have no acceptable fits with any of the four models. This means that 66% of the cases can be fitted with a

near-isothermal DEM model, 19% are best fitted with two isothermal components, most likely representing cases with two intersecting loops of different temperatures along the same line-of-sight (as verified in one case). Thus 85% of the cases are consistent with a single or a pair of isothermal loops. Only 15% of the cases could not be fitted with isothermal DEM models, but do not fit broadband Gaussian DEM models or six-point spline DEM models neither in 14% of all cases. This means that 14% need either a different DEM parameterization or have no DEM solution at all, because of errors in the total flux, background flux, or calibration of the filter response function.

The fact that the double-Gaussian DEM model performs better than the single-Gaussian or narrowband six-Gaussian DEM model is because the double-Gaussian DEM model has more flexibility to adjust to the main DEM temperature peak. The broadband six-Gaussian DEM model obviously does not describe most of the observed DEMs because they seem to be mostly dominated by narrowband temperature peaks. The statistics of the χ^2 -values of the 100 fits with 4 different DEM models is also listed in Table 3, showing the range of goodness-of-fit obtained in each time interval for the 10 loop locations. The double-Gaussian DEM model has the best statistics with $\chi^2 = 1.6 \pm 0.6$, while the single-Gaussian ($\chi^2 = 2.0 \pm 0.7$) and narrow six-Gaussian DEM Model ($\chi^2 = 2.3 \pm 1.0$) have an intermediate fit quality, and the broadband six-Gaussian DEM model ($\chi^2 = 3.8 \pm 1.7$) has the worst fit quality.

All 100 DEM fits of the double-Gaussian DEM model are shown in Fig. 7, grouped for each spatial location separately. Each panel in Fig. 7 shows the double-Gaussian DEM fit for 10 different times during one hour of observations. The time evolution of most loops appears to be gradual without changing the characteristics of the DEM model (except perhaps for events 211a and 335a). Most loops have a stable narrowband temperature structure of a primary loop, which occurs alone (events 131a, 171a, 94a, 171d), sometimes in presence of a weaker secondary loop with a different temperature (events 193a, 211a, 335a, 171b, 171c, 171e). None of the 100 cases exhibits a broadband temperature distribution, although the double-Gaussian DEM model can represent it with the free parameters of variable temperature widths (σ_{T1}, σ_{T2}).

In Fig. 8 we show a comparison of different DEM models for all cases with an acceptable goodness-of-fit, say $\chi^2 \leq 1.5$. In 23 cases (out of the 100 events) we find that at least 3 DEM models have an acceptable fit, which are shown in Fig. 8. The fact that these DEM models have all acceptable fits, although different parameterizations, implies that they are all consistent with the data, and thus reveal realistic uncertainties in the DEM definitions. Most cases show convergence to very similar single or multi-peaked DEM distributions. Only in 6 out of the 23 good solutions we find that a broadband DEM distribution is also consistent with the data, which is only the case if the other DEM models show a double or triple-peak solution, but never for a single-peak solution. Thus, there is no evidence for any single-peaked broadband DEM distribution, while ambiguities between multi-peaked narrowband and a single-peaked broadband DEM distribution exists only in very few cases. These results demonstrate a strong statistical trend of narrowband DEM distributions for loop cross-sections, similarly as found earlier with triple-filter analysis from TRACE data (Aschwanden and Nightingale 2005).

3.2. Physical Parameters

The statistical distributions of the best-fit parameters (of the strongest DEM temperature peaks) are shown in Fig. 9 in form of histograms, obtained from the 2-Gaussian DEM model. Loop temperatures were found with a mean and standard deviation of $\log(T_e) = 6.1 \pm 0.4$, which covers the entire range from $T_e = 0.4$ MK to $T_e = 5.0$ MK. The overabundance of loop temperatures in the temperature range of $T_e = 0.50 - 0.63$

MK is a selection effect, because we arbitrarily choose half of the identified loops in the 171 Å filter. The electron density is found in a range of $\log(n_e) = 8.9 \pm 0.2$, based on the measurements of the loop emission measure EM , width w , and assumption of unity filling factor,

$$n_e = \sqrt{\frac{EM}{w}} . \quad (11)$$

The loop widths were found in a range of $w = 2.9 \pm 0.8$ Mm, which corresponds to a range of $\approx 5 - 10$ pixels (Table 2).

3.3. Empirical Response Function for the 94 Å filter

The nominal response function of the AIA 94 Å filter as available in the *Solar Software (SSW)* package is known to be incorrect, according to information from James Lemen, Harry Warren, Joan Schmelz, Nancy Brickhouse, and Peter Beiersdorfer (private communication). The nominal 94 Å response function is shown in Fig. 10, which shows a double peak at $\log(T) \approx 6.1$ due to Fe X lines and at $\log(T) \approx 6.8$ due to Fe XVIII lines. AIA images in 94 Å often display strong emission from the $\log(T) \approx 6.0$ quiet corona that is in excess of the expected response function. It is therefore suspected that a large number of Fe X atomic transitions are not included in the currently available CHIANTI code, which is the atomic database of the AIA response function calculation. We experienced this problem directly in the sense that the flux observed in the 94 Å filter could not be matched with the nominal response function in our statistical DEM modeling of 100 mostly isothermal loop events.

In order to derive a first-order correction to the nominal 94 Å response function $R_{94}(T)^{nom}$ we defined an empirical boost factor q_{94} for the cool-temperature peak of the 94 Å response function, say at $\log(T) \leq 6.3$,

$$R_{94}(T)^{emp} = \begin{cases} q_{94} R_{94}(T)^{nom} & \text{for } \log(T) \leq 6.3 \text{ Å} \\ R_{94}(T)^{nom} & \text{for } \log(T) > 6.3 \text{ Å} \end{cases} \quad (12)$$

In order to determine the correction factor q_{94} we ran first all DEM fits for the selected 100 loop events with the free variable q_{94} in addition to the list of six free DEM parameters defined with Eqs. (7) and (8) and obtained a statistical distribution of best-fit values q_{94} with a mean and standard deviation of,

$$q_{94} = 6.7 \pm 1.7 , \quad (13)$$

which is shown in Fig. 10 (left). This correction factor is most accurately obtained from near-isothermal cases with temperatures around $\log(T) \approx 6.0$. We fixed then this correction factor to a constant value $q_{94} = 6.7$ and repeated all the fits with the corrected empirical response function $R_{94}(T)^{emp}$ specified in Eq. (12), leading to the results described in Section 3 and Figures 5-9.

There is also some concern about the accuracy of the 131 Å response function, where the ionization fractions for Fe VIII have been called into question. Young et al. (2007) have noted that Si VII and Fe VIII spectroheliograms look nearly identical despite the fact that these two ions are separated in temperature by 0.2 dex. However, we fitted our DEMs with and without the 131 Å channel without finding a significant difference.

4. DISCUSSION

We discuss our results in view of instrumental biases, such as the background subtraction issue (Section 4.1), the narrowband temperature filter bias (Section 4.2), and put the results in context of physical loop models (Section 4.3).

4.1. The Loop and Background Co-spatiality Issue

The thermal structure of an individual coronal loop can only be properly determined if the loop-associated EUV flux $F_{\lambda}^{loop} = F_{\lambda}^{tot} - B_{\lambda}$ is accurately separated from the background flux B_{λ} along each line-of-sight. The background corona is multi-thermal, since it consists of tens to thousands of other loops along each line-of-sight, any contamination of loop fluxes F_{λ}^{loop} with background fluxes B_{λ} will add also a multi-thermal contribution to the resulting DEM. Quantitative modeling of the multi-loop background corona that reproduces the observed DEMs has been performed with the *CELTIC* model (Aschwanden et al. 2007). The best background subtraction is achieved when the background is evaluated cospatially to the loop, say with a linear interpolation between the left and right-hand side of a loop cross-section, which is essentially the technique we applied in our study here. Other methods that estimate the background flux not cospatially to the loop are fundamentally flawed, because the coronal flux at two different locations is unrelated to each other. It is therefore imperative to provide the location and definition of background fluxes in loop studies.

A recent study analyzed a coronal loop with AIA, observed on 2010 Aug 3, and carried out some DEM modeling, claiming a multithermal rather than an isothermal DEM distribution (Schmelz et al. 2010). Unfortunately this study does not specify the loop coordinates, total fluxes, background fluxes, or background locations. The description that *10 pixels from a clean background area* were subtracted from the loop fluxes suggests a non-cospatial determination of loop and background fluxes, which most likely contributes a multi-thermal contamination to the loop and this way explains the inferred result of a multithermal loop. The cospatial total fluxes F_{λ}^{tot} and background fluxes B_{λ} shown for 100 loop events in Fig. 5 demonstrate that fluxes from the most obvious (foreground) loops amount only to about 5% – 50% of the total flux in each pixel, and thus a slight contamination changes the flux ratios in different filters and the resulting DEMs significantly. A fit of a broadband DEM with a temperature width of $\Delta \log(T) \approx 0.6$ is shown in Fig. 4 of Schmelz et al. (2010), which obviously fits better than a narrowband DEM. However, the inferred DEM applies not to the loop alone, but rather to a combination of the target loop plus an unknown fraction of the background corona. Our results of dominantly narrowband DEMs for 100 loop events is therefore not in conflict with that study, because we would obtain similar broadband DEMs with non-cospatial background estimates.

4.2. Narrowband and Broadband Temperature Diagnostics

The issue of the inadequacy of temperature measurements in the solar corona through narrowband filter and line ratios was raised in Martens et al (2002), where it was argued that recently discovered isothermal loops could be an artifact of narrowband filter methods. This criticism indeed needs to be taken seriously, because data with a narrow temperature coverage may not have sufficient flexibility to reconstruct broadband-temperature DEM distributions, such as triple-filter data from TRACE within a combined temperature range of $T \approx 0.7 - 2.7$ MK. Although instruments with a broader temperature

range exist (e.g., SoHO/CDS or Hinode/EIS), reliable multi-wavelength modeling is extremely difficult due to insufficient spatial resolution, inconsistent instrument calibrations, non-overlapping time coverage, and image distortion of scanning spectrographs. A single instrument such as SDO/AIA with a sufficient large number of temperature filters, self-consistent calibration, high spatial resolution, temporal simultaneity, and sufficient cadence is therefore the first good opportunity to attempt reliable multi-temperature modeling of coronal loops.

Despite the incompleteness of the 94 Å response function, which we bootstrapped with self-consistent solutions with the other 5 coronal AIA filters, AIA essentially allows us to model DEMs in a temperature range of $\log(T) \approx 5.7-7.2$ (or $T = 0.5-16$ MK), which spans a logarithmic range of 1.5 decades. The average temperature spacing is $\Delta\log(T) \approx 1.5/6 = 0.25$ dex, which defines a temperature resolution with a Gaussian width of $\sigma_T \approx 0.1$ dex. We have chosen 4 different parameterizations of DEM distributions that can resolve narrowband temperature peaks down to this resolution of $\sigma_T \gtrsim 0.1$, and at the same time can represent broad distributions up to the full temperature sensitivity range of $\Delta\log(T) \approx 1.5$ dex. Interestingly, the majority of reconstructed DEMs converged to narrowband temperature peaks near $\sigma_T \approx 0.1$ dex (Fig. 9), especially those DEMs with the most reliable goodness-of-fit χ^2 -values ($\chi^2 = 1.6 \pm 0.6$, see Table 3 for double-Gaussian DEMs). A similar result was found with TRACE triple-filter DEM modeling, where 84% of acceptable DEMs (with $\chi^2 \leq 1.5$) were found to be isothermal (Aschwanden and Nightingale 2005), despite of the smaller number of available temperature filters. Could these results be an artifact of the numerical forward-fitting code? The fact that 3 different DEM parameterizations converge all to the same narrow-temperature peaks seems to rule out a numerical artifact. The only DEM parameterization that we did not allow to converge to narrowband temperature solutions (i.e., the broadband six-Gaussian DEM function with Gaussian widths of $\sigma_T = 0.5$), converged in almost all cases to a DEM solution with a much poorer goodness-of-fit χ^2 -value ($\chi^2 = 3.8 \pm 1.7$, see Table 3 for broadband six-Gaussian DEMs). It therefore appears that broad DEM distributions are very atypical for single loops after proper (cospatial) background subtraction, unless multiple loops intersect each other cospatially. This explains the double-peak DEM distributions we found in half of the analyzed cases (see Fig. 7). Our AIA results are also consistent with a study using EIS/Hinode (Warren et al. 2008), where a set of 20 coronal loops was found to be isothermal within a very narrow temperature distribution of $\Delta T \lesssim 0.3$ MK at $T \approx 10^{6.1} - 10^{6.2}$ K ≈ 1.4 MK, which corresponds to a Gaussian width $\sigma_{\log(T)} = \log(T + \sqrt{2}\Delta T) - \log(T) \approx 0.11$ dex. In comparison, our result shows an upper limit of $\sigma_{\log(T)} \gtrsim 0.11 \pm 0.02$ (Fig. 9). Our results are also consistent with Hinode/EIS spectroscopic observations that revealed near-isothermal upflows in active region loops (Tripathi et al. 2009).

All these results suggest that AIA enables us reliably to reconstruct DEMs in a temperature range of $\Delta\log(T) \lesssim 1.5$ with a resolution of $\Delta\log(T) \gtrsim 0.25$, if loops can be properly separated from the cospatial coronal background. However, limitations exist when the cospatial cross-sectional background profile significantly deviates from a linear interpolation, or when substantial density and temperature gradients along the averaged loop segment exist, in which case a self-consistent DEM solution may be inhibited. In addition, the Poissonian photon noise and calibration errors contribute to the uncertainty of DEM fits.

4.3. Isothermal versus Multi-thermal Loop Models

How do we explain the result of predominant isothermal loops in terms of physical models? Let us first discuss isothermality in terms of nanoflare models. Since nanoflares occur on unresolved spatial scales and have no cross-field transport, every nanoflare model predicts a highly inhomogeneous density and temperature structure of macroscopic loops (Klimchuk 2006). The only way to make a nanoflaring loop structure more

isothermal is to synchronize a storm of nanoflares and to streamline them to identical energy outputs, so that their release appears to be simultaneous and homogeneous across a loop cross-section, which in the continuum limit is macroscopically indistinguishable from a monolithic loop. Following Occam’s razor, assuming a coherent isothermal upflow in a single flux tube is a weaker assumption than synchronized upflows with equal temperatures in a multi-thread structure. However, a stronger argument that currently supports a fragmented energy release, such as nanoflares, is the observed lifetime of some coronal loops that are more extended than expected for an impulsive heating phase with subsequent cooling (e.g., Warren et al. 2008). However, the time evolution of isolated loop strands has first to be studied with high spatial resolution and high time cadence in many temperature filters, such as AIA provides, before clear-cut cases can be established. At this point we can only conclude that the observed isothermality of coronal loops is not consistent with standard nanoflare scenarios, nor do nanoflare models explain or predict the isothermal property.

If an isothermal loop cross-section cannot be produced by nanoflares, what other physical process can account for it? The most natural mechanism seems to be that of chromospheric evaporation as known in flares (e.g., Antonucci et al. 1999), where either coronal or chromospheric magnetic reconnection processes cause a local heating of the chromosphere and drive coherent upflows of heated plasma into a coronal loop conduit. Although the details of the heating cross-section transverse to the magnetic field is not fully understood, flare observations yield clear evidence that postflare loops are filled impulsively with heated plasma over a cross-section of several thousand kilometers. Distributions of hard X-ray footpoint sources in flare loops have typical FWHM of $\approx 2'' - 8''$, or $w \approx 1.5 - 6.0$ Mm, according to RHESSI measurements with a spatial resolution of $\approx 2''$ (Dennis and Pernak 2009). One of the few flare observations that resolve the blue-shifted upflows from near-cospatial red-shifted downflows is described in Czaykowska et al. (1999), which yields evidence for coherent near-isothermal upflows over a cross-section of $\approx 4''$ ($\lesssim 3$ Mm). Similarly, Hinode/EIS spectroscopic observations showed near-isothermal upflows in active region loops (Tripathi et al. 2009). The heating process at a cospatial location lasts in the order of minutes for flare loops, while a flare can last for hours, with the energy release propagating along and perpendicular to the neutral line. Of course, the upflows in flare loops are more or less continuous during the heating phase, and thus no thermal equilibrium is reached that obeys the theoretically expected conductive and radiative cooling times, explaining the discrepancies between observed loop lifetimes and theoretically calculated cooling times (Warren et al. 2008). The temperature of an arbitrary loop cross-section can be nearly constant during some part of the heating phase due to the continuous upflow of isothermal plasma, which explains the slow time evolution observed in coronal loops during time intervals of hours (see Fig. 7). It seems natural to suggest a flare-like heating mechanism for active region loops, although there might be significant differences. While the coronal height of magnetic reconnection regions is established in solar flares (e.g., Masuda et al. 1995), reconnection processes may happen in the chromosphere and transition region (Aschwanden et al. 2007; Gudiksen and Nordlund 2005a,b), causing subsequent upflows of heated plasma into the coronal parts of active region loops. It is too early to speculate about the details of the generic heating mechanism of active region loops, before we analyzed comprehensive multi-wavelength observations of coronal loops such as with AIA and modeled their hydrodynamic evolution self-consistently.

5. CONCLUSIONS

Our study of the cross-sectional temperature structure of coronal loops using AIA six-filter data leads us to the following conclusions:

1. From an sample of 100 loop snapshots measured at 10 different locations and at 10 different times in an active region near disk center, we measured the cross-sectional flux profiles in 6 coronal temperature filters, subtracted a cospatial linearly interpolated background, and reconstructed the differential emission measure (DEM) distributions in the temperature range of $T \approx 0.5 - 16$ MK. We found dominantly narrowband peak temperature components with a thermal width of $\sigma_{\log(T)} \leq 0.11 \pm 0.02$, close to the temperature resolution limit of the instrument ($\sigma_{\log(T)} = 0.1$). This result, derived from 6-filter data, is consistent with similar analysis from TRACE triple-filter data (Aschwanden and Nighthale 2005) and from EIS/Hinode data (Warren et al. 2008; Tripathi et al. 2009).
2. The DEM distribution was modeled with 4 different parameterizations, including one or two Gaussians with free parameters and six-Gaussian functions with narrowband ($\sigma_{\log(T)} \geq 0.1$) and broadband ($\sigma_{\log(T)} \geq 0.1$) temperature components. Among the subset of DEM solutions with acceptable goodness-of-fit ($\chi^2 < 2$) we find that the observed fluxes can be fitted with a single-Gaussian DEMs in 66%, with double-Gaussian DEMs in 19%, while 14% could not be fitted with any of the four DEM models, which might have no DEM solution because of errors in the 6 filter fluxes, backgrounds, or in the calibration. The cases with double-Gaussian DEMs are most likely attributed to a pair of loops that intersects at the same line-of-sight.
3. The nominal response function of the AIA 94 Å filter is found to be inconsistent with the other 5 coronal temperature filters in the low-temperature part of $\log(T) \lesssim 6.3$. From self-consistent fits of 100 mostly isothermal loop events we establish an empirical response function where the low-temperature response is boosted by an average correction factor of $q_{94} = 6.7 \pm 1.7$, which is consistent with the known deficiency of missing Fe X lines in the Chianti code.
4. The main result of near-isothermal loop structure in this random sample of 100 loop snapshots provides a strong argument for a coherently operating heating mechanism across the observed macroscopic loop structures with a width of $w \approx 2 - 4$ Mm. The observed isothermality of coronal loops is not consistent with standard nanoflare scenarios, nor do nanoflare models explain or predict the isothermal property. Flare-like heating mechanisms that drive chromospheric evaporation and upflow of heated plasma into coronal loops are known to produce near-isothermal loop cross-sections, and thus may be a also a viable mechanism for heating of active region loops.

Future loop studies with AIA are anticipated that determine the thermal loop structure along the loop axis, as well as a function of time, which will provide unprecedented input for hydrodynamic simulations of loops. Time-dependent hydrodynamic models will allow us then to deconvolve the temporal and spatial heating function, which ultimately will lead to the identification of coronal heating mechanisms.

Acknowledgements: This work is partially supported by NASA under contract NNG04EA00C of the SDO/AIA instrument.

Appendix A : Testing the Inversion of DEM Distributions

In order to test the reliability of our DEM inversion code we perform a test by simulating a set of 21 DEM distributions that contain one or two Gaussian peaks, which are then converted into loop cross-sectional flux profiles $F_{\lambda}^{tot}(x)$ of the 6 AIA filters λ , with photon noise added, and inverted with our forward-fitting model with the double-Gaussians DEM model (Eq. 7). Assuming that we averaged the flux values of the

loop cross-sections over a loop length segment of $n_s = 50$ AIA pixels, the photon noise is reduced by a factor of $1/\sqrt{n_s} \approx 1/7$ with respect to the photon noise in a single pixel. In the simulated DEMs we choose double peaks with peak temperatures $T_i = 10^{5.6+0.2*i}$ for $i = 1, \dots, 6$. There are 6 single-peak cases and $(6 \times 5)/2 = 15$ double-peak cases, hence a total of 21 cases, numbered consecutively in Fig. 11 in order of increasing separation of the temperature peaks. The Gaussian widths of all components is $\sigma_{\log(T)} = 0.1$. The emission measures were chosen as $EM_1 = 10(T_i/T_0)^4 \text{ DN s}^{-1}$ for the first peak, and $EM_2 = EM_1/2$ for the second peak, following the Rosner-Tucker-Vaiana scaling law ($EM \propto T^4$), in order to reproduce typical emission measures. The loop width was chosen to correspond to 5 AIA pixels, and the fitted cross-sectional profiles contain $n_w = 20$ AIA pixels in width and $n_s = 50$ AIA pixels in length.

The results of the inversion and the goodness-of-fit χ_{red}^2 are shown in Fig. 12. We started with initial guess values in the forward-fitting code based on the input flux values and obtained an acceptable fit of $\chi_{red}^2 \lesssim 2.0$ in most cases. In those cases where no acceptable fit was found in the first trial, we iterated the initial guesses of the temperature values randomly in the range of $T = 1 - 10$ MK until we obtained an acceptable fit with χ_{red}^2 , which was achieved for all cases. The mean and standard deviation of the goodness-of-fit values is $\chi_{red}^2 = 1.33 \pm 0.25$ for the 21 cases shown in Fig. 11. Therefore, we conclude that our forward-fitting code reliably retrieves the DEM distributions within the uncertainty of the data noise, in theory. Practically, there are errors in the measurement of the total fluxes, background fluxes, and calibration that are not part of this simulation.

REFERENCES

- Antonucci,E., Alexander,D., Culhane,J.L., DeJager,C., MacNeice,P., Somov,B.V., and Zarro,D.M. 1999, *Chapter 10: Flare dynamics*, in *The Many Faces of the Sun: A Summary of the Results from NASA's Solar Maximum Mission*, (eds. Strong,K.T., Saba,J.L.R., Haisch,B.M., and Schmelz,J.T.) 610p., Springer, Berlin, p.331.
- Aschwanden, M.J., Winebarger, A., Tsiklauri, D., and Peter, H. 2007, *Astrophys. J.* 659, 1673.
- Aschwanden, M.J. and Nightingale, R.W. 2005, *Astrophys. J.* 633, 499.
- Aschwanden, M.J. 2006, *Physics of the Solar Corona - An Introduction with Problems and Solutions*, Springer/Praxis, New York, ISBN 3-540-30765-6, paperback, 892p.
- Aschwanden, M.J., Nightingale, R.W., and Boerner, P. 2007, *Astrophys. J.* 656, 577.
- Boerner, P., Edwards, C., Lemen, J., Rausch, A., Schrijver, C., Shine, R., Shing, L., Stern, R., Tarbell, T., Title, A., and Wolfson, C.J. 2011, *Initial calibration of the Atmospheric Imaging Assembly Instrument*, (in preparation).
- Czaykowska, A., De Pontieu, B., Alexander, D., and Rank, G. 1999, *Astrophys. J.* 521, L75.
- Del Zanna, G. and Mason, H.E. 2003, *Astron. Astrophys.* 406, 1089.
- Dennis, B.R. and Pernak, L. 2009, *Astrophys. J.* 698, 2131.
- Gburek, S., Sylwester, J., and Martens, P. 2006, *Solar Phys.* 239, 531.
- Gudiksen, B.V., and Nordlund, A. 2005a, *Astrophys. J.* 618, 1020.
- Gudiksen, B.V., and Nordlund, A. 2005b, *Astrophys. J.* 618, 1031.

- Judge, P.G. 2010, *ApJ* 708, 1238.
- Klimchuk, J.A. 2006, *Solar Phys.* 234, 41.
- Lemen, J. and AIA Team, 2011, *Solar Phys.* (in preparation).
- Martens, P.C.H., Cirtain, J.W., and Schmelz, J.T. 2002, *Astrophys. J.* 577, L115.
- Masuda, S., Kosugi, T., Hara, H., Sakao, T., Shibata, K., and Tsuneta, S. 1995, *PASJ* 47, 677.
- O’Dwyer, B.O., Del Zanna, G., Mason, H.E., Weber, M.A., and Tripathi, D. 2010, *A&A* (subm).
- Parker, E.N. 1988, *Astrophys. J.* 330, 474.
- Press, W.H., Flannery, B.P., Teukolsky, S.A., and Vetterling, W.T. 1986, *Numerical Recipes - The Art of Scientific Computing*, Cambridge University Press, Cambridge.
- Schmelz, J.T., Naraoui, K., Rightmire, L.A., Kimble, J.A., Del Zanna, G., Cirtain, J.W., DeLuca, E.E., and Mason, H.E. 2009, *Astrophys. J.* 691, 503.
- Schmelz, J.T., Kimble, J.A., Jenkins, B.S., Worley, B.T., Anderson, D.J., Pathak, S., and Saar, S.H. 2010, *Astrophys. J.* 725, L34.
- Tripathi, D., Mason, H.E., Dwivedi, B.N., DelZanna, G., and Young, P.R. 2009, *ApJ* 694, 1256
- Warren, H.P., Ugarte-Urra, I., Doschek, G., Brooks, D.H., and Williams, D.R. 2008, *Astrophys. J.* 686, L131.
- Young, P.R., DelZanna, G., Mason, H.E., Dere, .P., Landi, E., Landini, M., Doschek, G.A., Brown, C.M., Culhane, L., Harra, L.K., Watanaba, T., and Hisohisa, H. 2007, *Publ. Astron. Soc. Japan* 59, S857.

Table 1. AIA/SDO wavelength bands.

channel name	Primary ions	Characteristic log(T)
white light	continuum	3.7
1700 Å	continuum	3.7
304 Å	He II	4.7
1600 Å	C IV+cont.	5.0
171 Å	Fe IX	5.8
193 Å	Fe XII, XXIV	6.1, 7.3
211 Å	Fe XIV	6.3
335 Å	Fe XVI	6.4
94 Å	Fe XVIII	6.8
131 Å	Fe VIII, XXI	5.6, 7.1

Table 2. Center coordinates (at reference time 2010 Jul 24, 21:00 UT), lengths, and widths of selected loops.

Loop name	Position (x_0, y_0) (pixels)	Segment length (n_s) (pixels)	Segment width (n_w) (pixels)	Loop width w (pixels)
131a	(140,404)	21	20	8.2
171a	(463,264)	89	20	8.1
193a	(235,218)	35	28	8.0
211a	(298,286)	20	20	4.9
335a	(329,296)	21	20	6.9
94a	(302,417)	30	20	9.7
171b	(150,266)	33	20	7.2
171c	(203,425)	30	20	5.8
171d	(462,235)	25	20	4.7
171e	(112,431)	34	20	7.5

Table 3. Range of goodness-of-fit χ^2 -values obtained for the time range of 2010 Jul 24, 21:00-22:00 UT for each of the 10 loop positions and 4 different DEM models.

Loop name	1-Gaussian DEM	2-Gaussian DEM	Narrow 6-Gaussian DEM	Broad 6-Gaussian DEM
131a	1.32– 2.40	1.09– 1.86	1.16– 1.99	1.73– 3.77
171a	1.54– 3.10	1.44– 2.86	1.75– 3.73	2.58– 6.52
193a	1.63– 2.97	1.48– 1.75	1.79– 3.33	2.37– 5.76
211a	1.39– 3.57	1.14– 3.78	1.99– 3.61	5.44– 7.76
335a	1.90– 3.28	1.14– 2.79	1.94– 4.58	3.03– 6.43
94a	1.26– 4.09	1.13– 3.83	1.86– 7.60	3.50– 6.36
171b	1.21– 1.62	1.09– 1.39	1.09– 1.35	1.16– 1.72
171c	1.08– 1.89	1.08– 1.67	1.08– 1.91	1.41– 4.14
171d	1.33– 1.98	1.16– 1.76	1.52– 4.42	1.54– 3.78
171e	1.15– 1.51	1.11– 1.46	1.17– 1.61	2.74– 5.15
Average	1.95±0.68	1.59±0.58	2.27±1.06	3.76±1.70

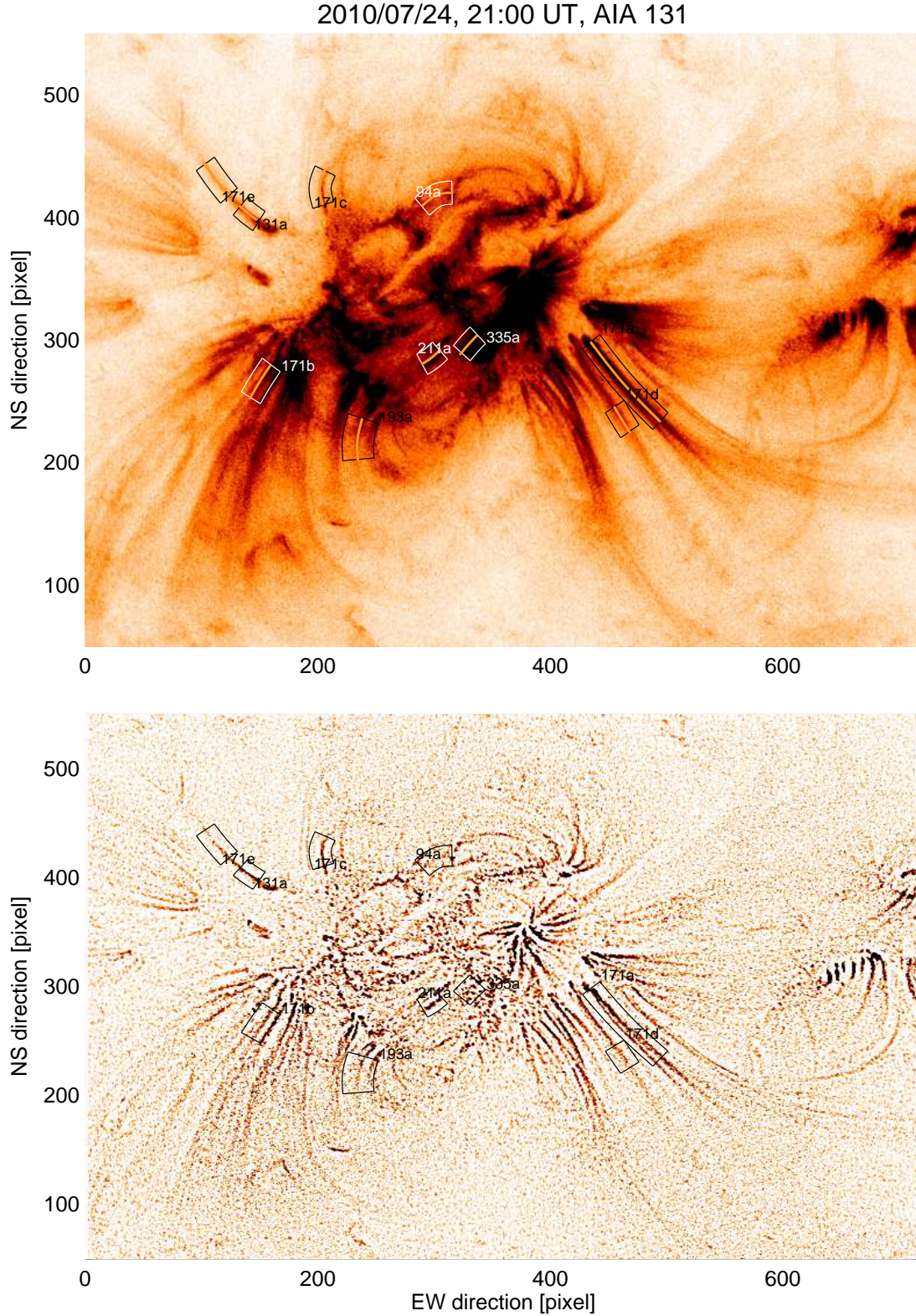


Fig. 1.— Partial AIA image observed at 171 Å on 2010 July 24, 21:00 UT, rendered with inverse greyscale (top) and as a highpass-filtered version (by subtracting the original image smoothed with a boxcar of 7×7 pixels). The location of the extracted loop segment boxes are indicated, which are curved arrays aligned with the loop spines at the 10 selected loop locations. The background fluxes are interpolated between the boundaries of the boxes on both sides of the loop spines.

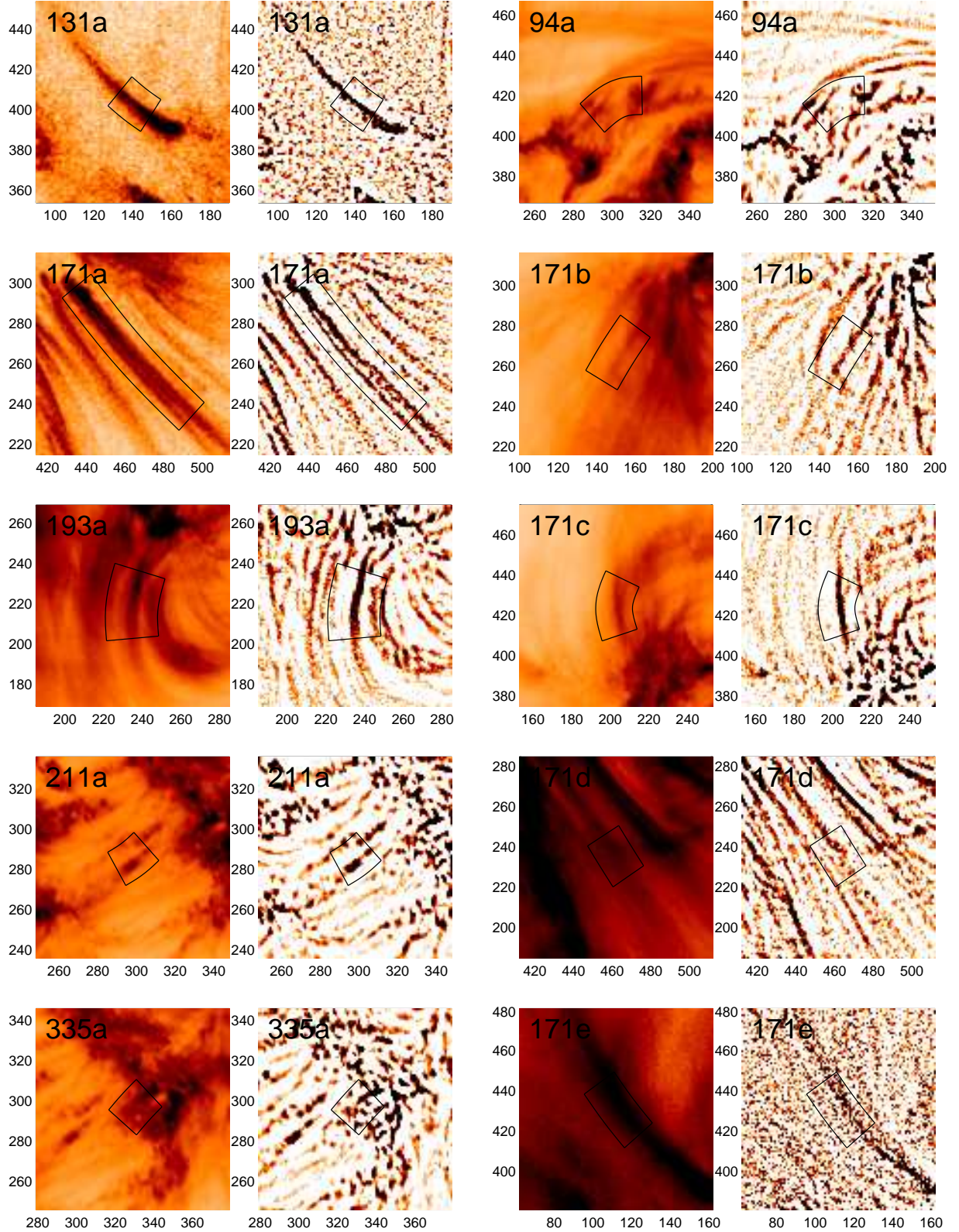


Fig. 2.— Enlargements of 100×100 pixel subimages around the selected 10 loops, extracted from the same AIA 171 Å image as shown in Fig. 1, observed on 2010 July 24, near 21:00 UT.

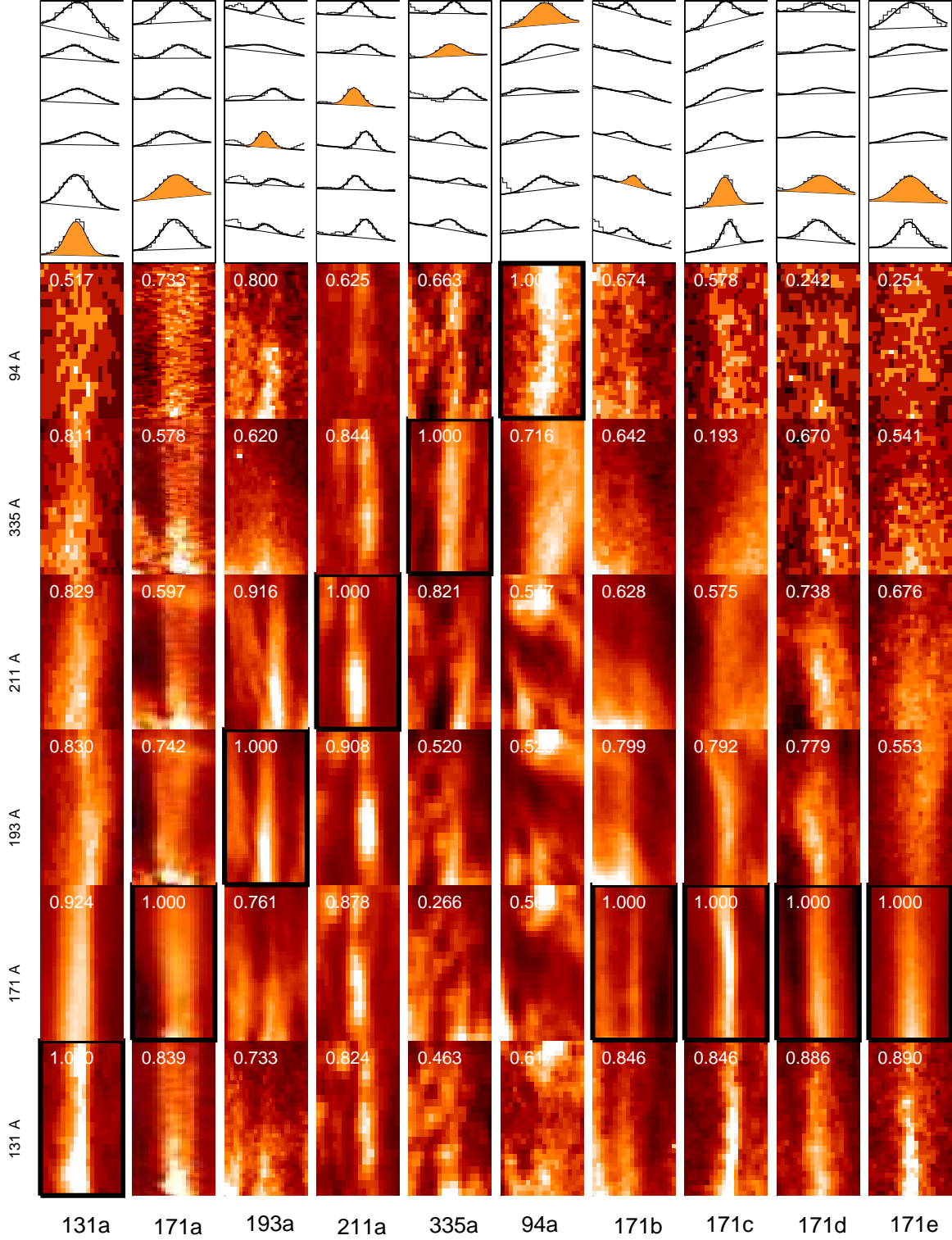


Fig. 3.— Stretched-out loop segments aligned with the loop spine (in vertical direction) for 10 loop segments at the first of the 10 time intervals, shown for all 6 coronal filters. The cross-sectional flux profiles $F_{\lambda}(x)$ in all 6 filters are shown in the top part. The wavelengths in which each loop was detected are indicated with a black frame and with a grey-colored cross-section. The cross-correlation coefficients between the partial image of each wavelength with the wavelength of detection are indicated in each partial image.

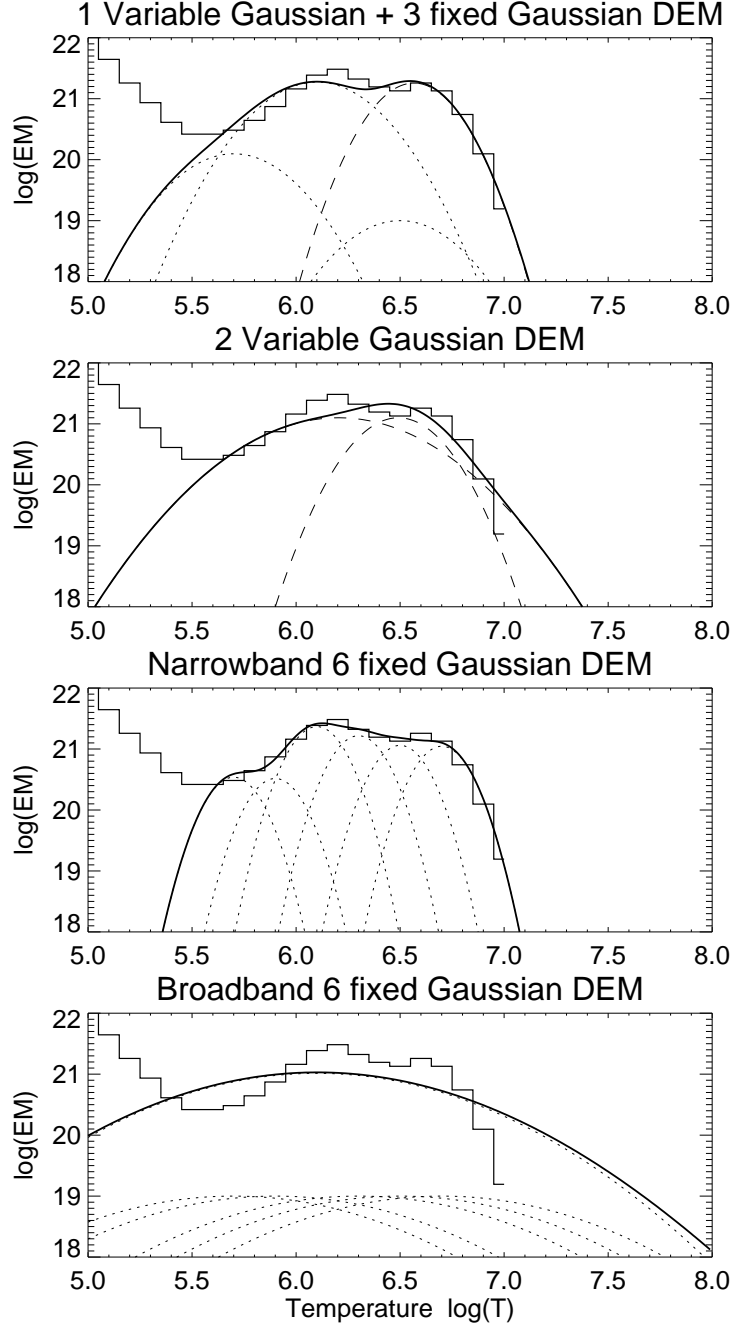


Fig. 4.— An observed DEM (histogram) from Brosius et al. (1996), labeled as AR 93, is fitted with our four different DEM parameterizations (Eq. 7). The best-fit DEM models are marked with thick solid lines, the variable Gaussian components (with three free parameters (EM_i, T_i, σ_T)) are marked with dashed curves, and the fixed Gaussians (EM_i variable, but T_i and σ_{T_i} are fixed) are marked with dotted curves. Note that the first 3 models with narrowband Gaussians ($\sigma_T \geq 0.1$) can represent the observed DEM with reasonable accuracy, while the broadband Gaussian model $\sigma_T = 0.5$ fails (bottom).

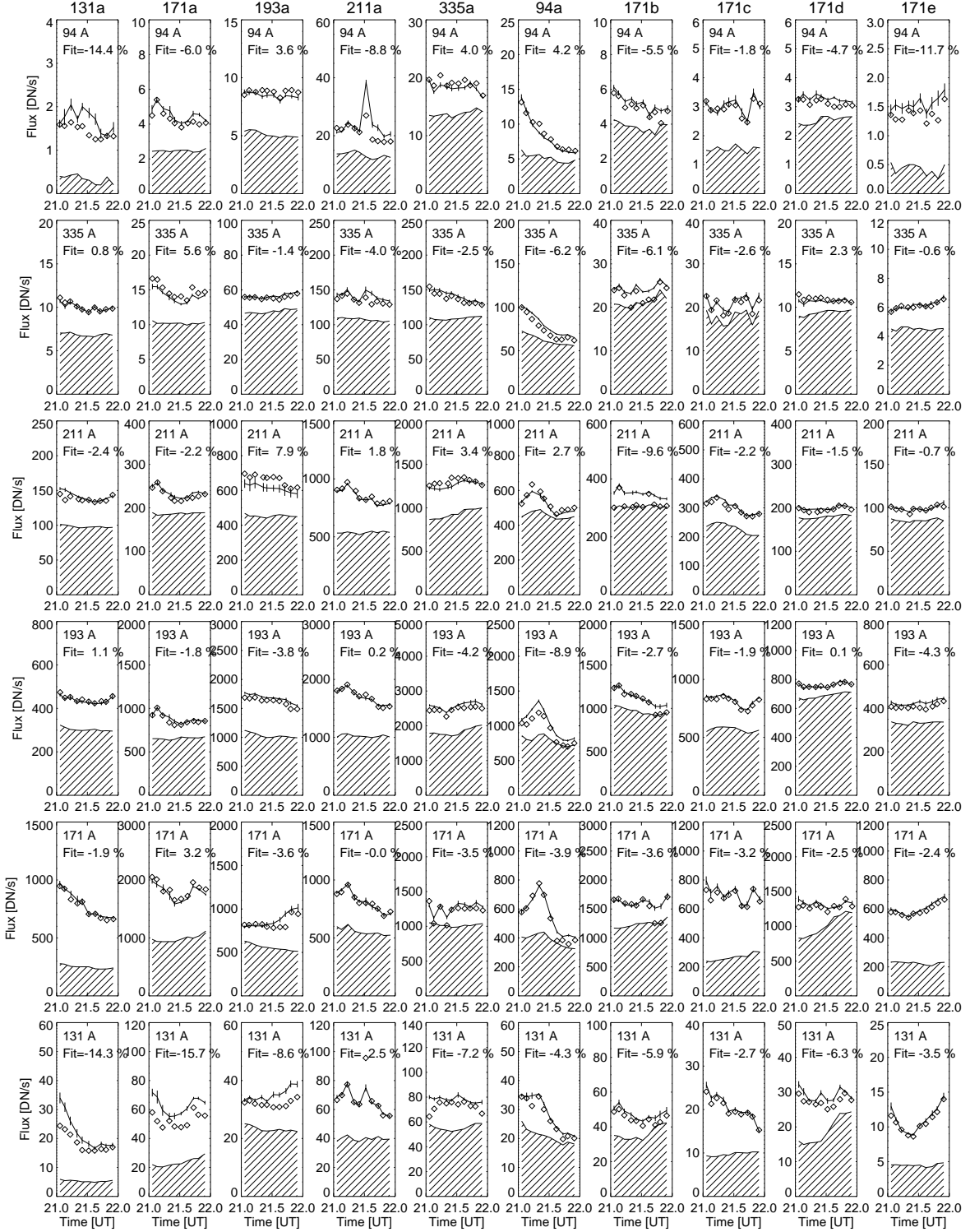


Fig. 5.— Time profiles of background fluxes $B_{\lambda}(t)$ (hatched), total fluxes $F_{\lambda}(t)$ (solid curve with error bars), and best fits $F_{\lambda}^{mod}(t)$ with the 2-Gaussian DEM model in 6 wavelengths (sequence in vertical direction) for 10 different loop positions (sequence in horizontal direction). The wavelength λ and fit accuracy (in percents) is indicated in each panel.

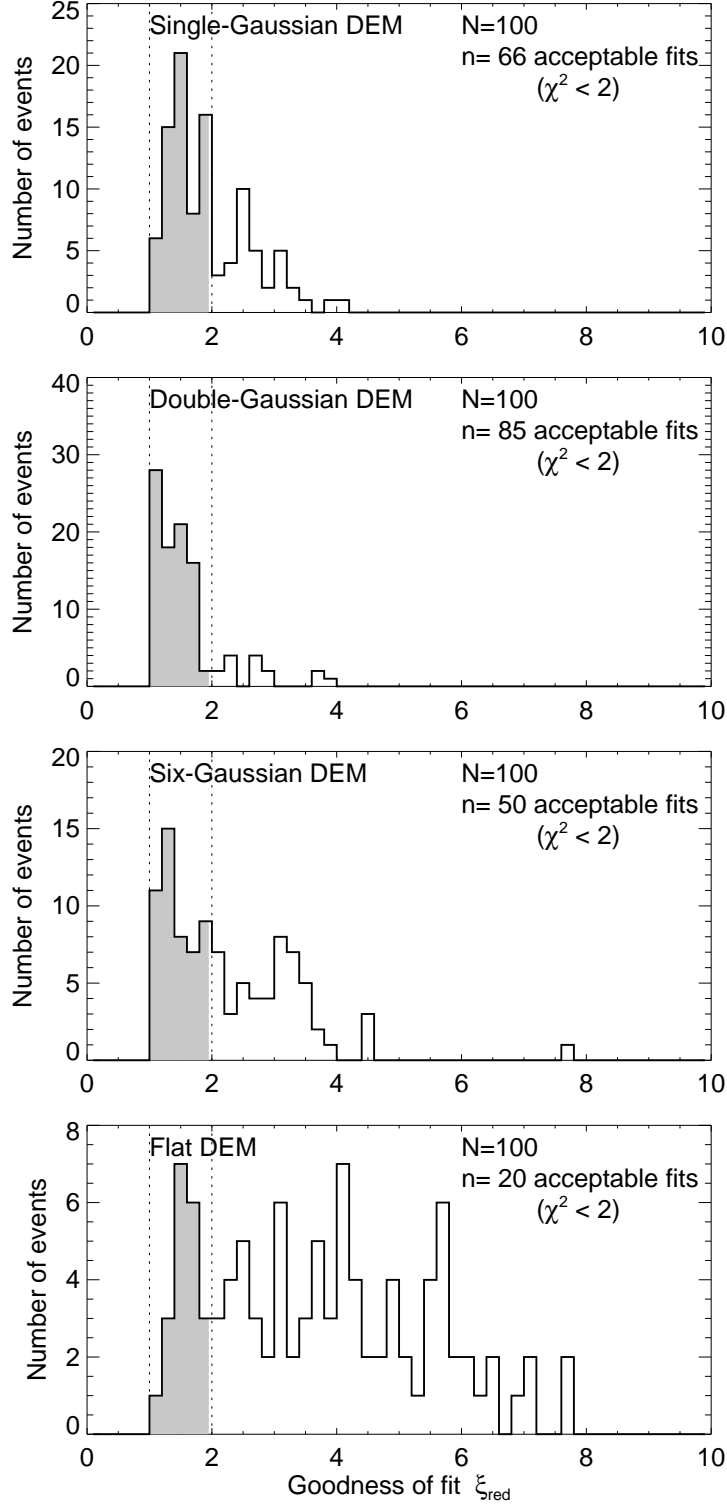


Fig. 6.— Histograms of the goodness-of-fit χ^2 -criterion for the 4 different DEM models: single-Gaussian (top); double-Gaussian (second); six-Gaussian (third); and flat DEM (bottom). Note that all models yield $\chi^2 > 1$, but only the double-Gaussian model contains most values (81%) within an acceptable range of $\chi^2 < 2$.

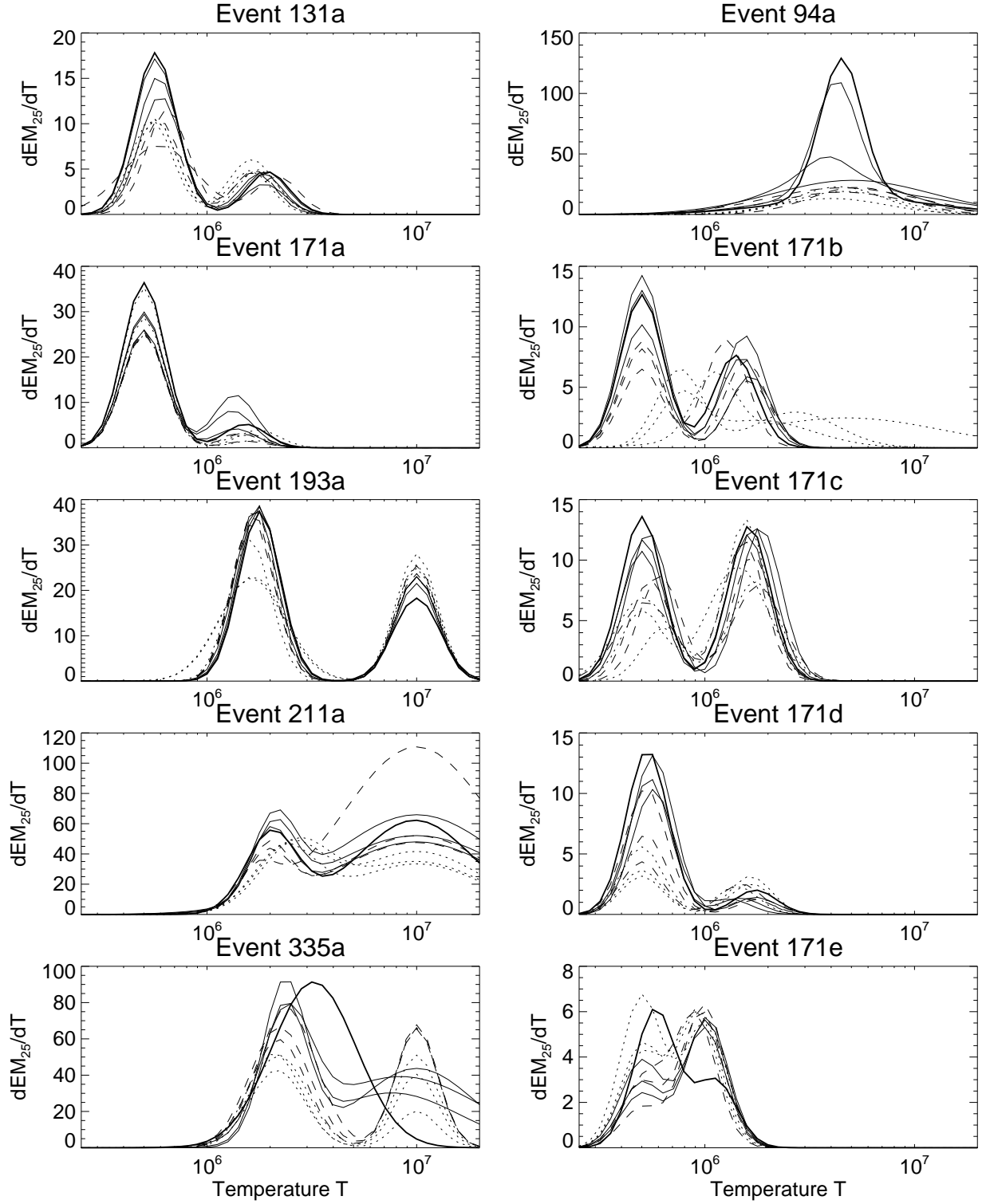


Fig. 7.— Differential emission measure (DEM) distributions fitted with the 2-Gaussian DEM model for the 10 different locations (each frame) in time steps of 6 minutes during the time interval of 2010 Jul 24, 21:00-22:00 UT. The first time frame corresponds to the detection time of a loop (first time step), time steps 2-4 are shown with solid linestyle, time steps 5-7 with dashed linestyle, and time steps 8-10 with dotted linestyle. Note the continuous evolution of the best-fitt DEMs.

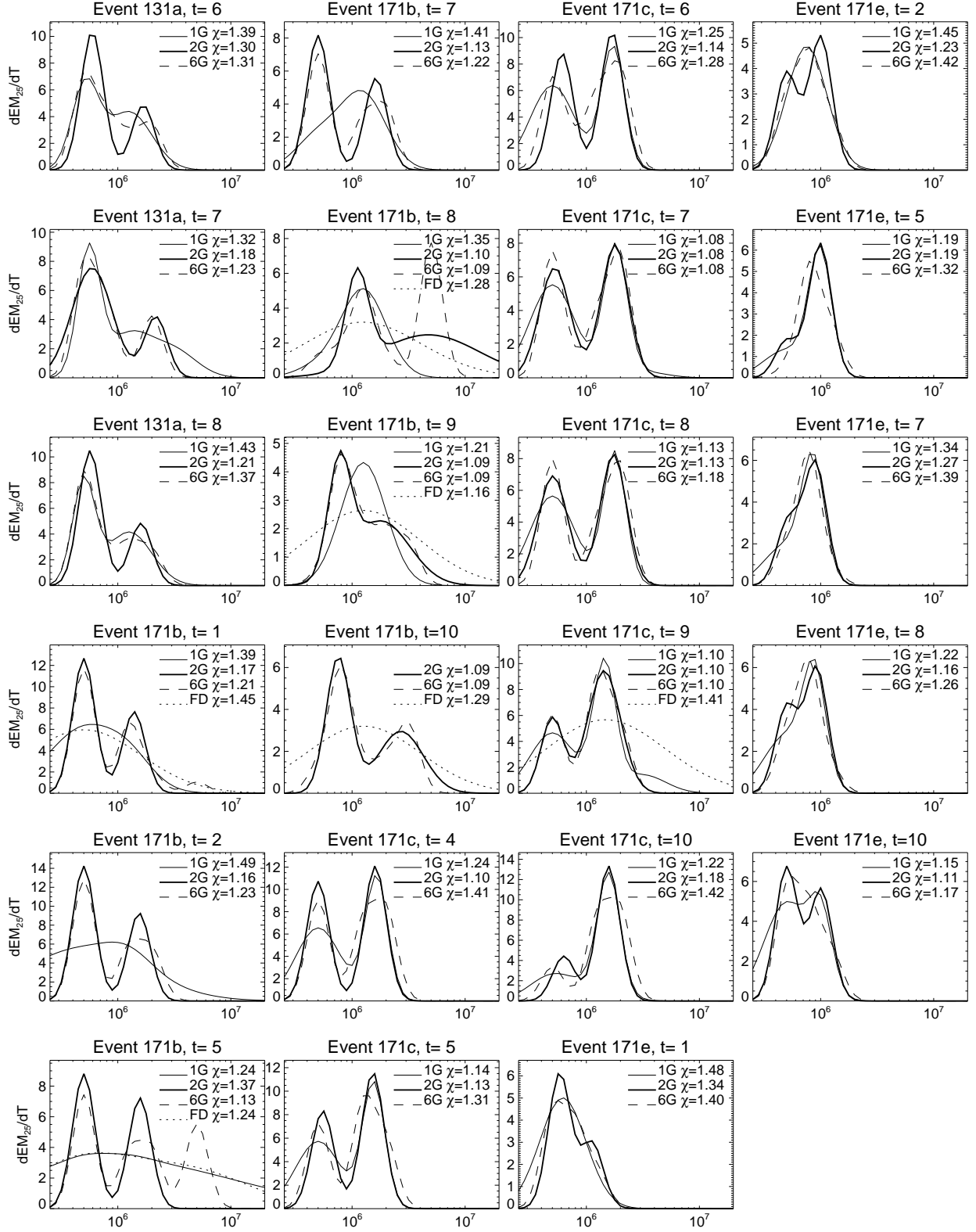


Fig. 8.— DEM solutions are shown for events where at least 3 different DEM models yield a goodness-of-fit of $\chi^2 \leq 1.5$, which is the case for 23 out of the 100 events. The 4 different DEM models are: single-Gaussian (thin solid line), double-Gaussian (thick solid line), narrowband six-Gaussian (dashed line), and broadband six-Gaussian DEM model (dotted line).

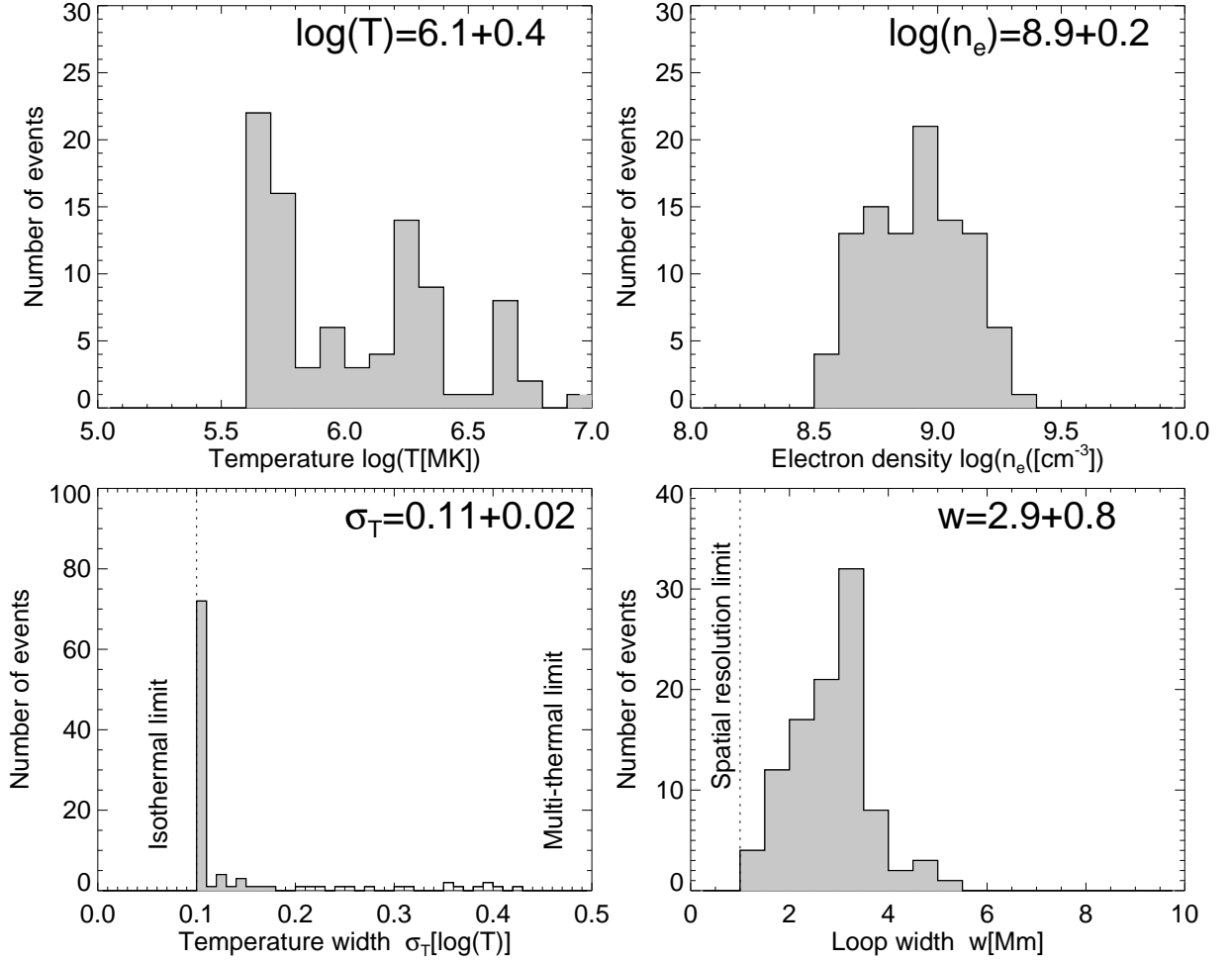


Fig. 9.— Parameter distributions of the principal DEM component measured with the 2D-Gaussian DEM model: the loop temperature $\log(T)$ (top left), the electron density $\log(n_e)$ (top right), the logarithmic temperature width σ_T (bottom left), and the loop width w (bottom right).

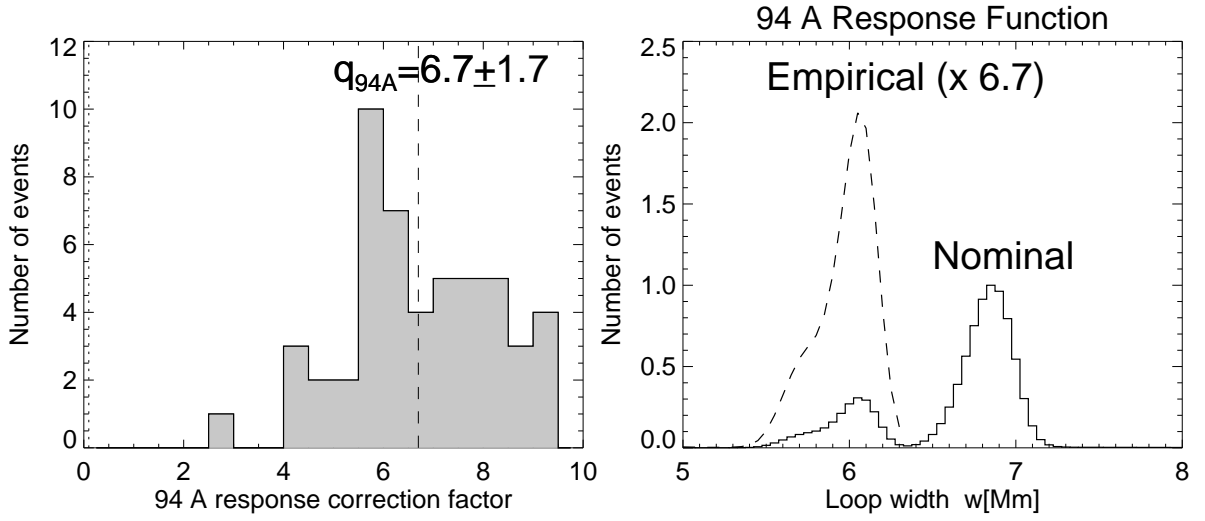


Fig. 10.— Empirical correction of AIA94 Å response function for the low-temperature response at $\log(T) < 6.3$ (right panel). The low-temperature response needs to be boosted by a factor of 6.7 ± 1.7 according to best-fit DEM solutions obtained from 100 DEM fits using a 2-Gaussian DEM model (left panel).

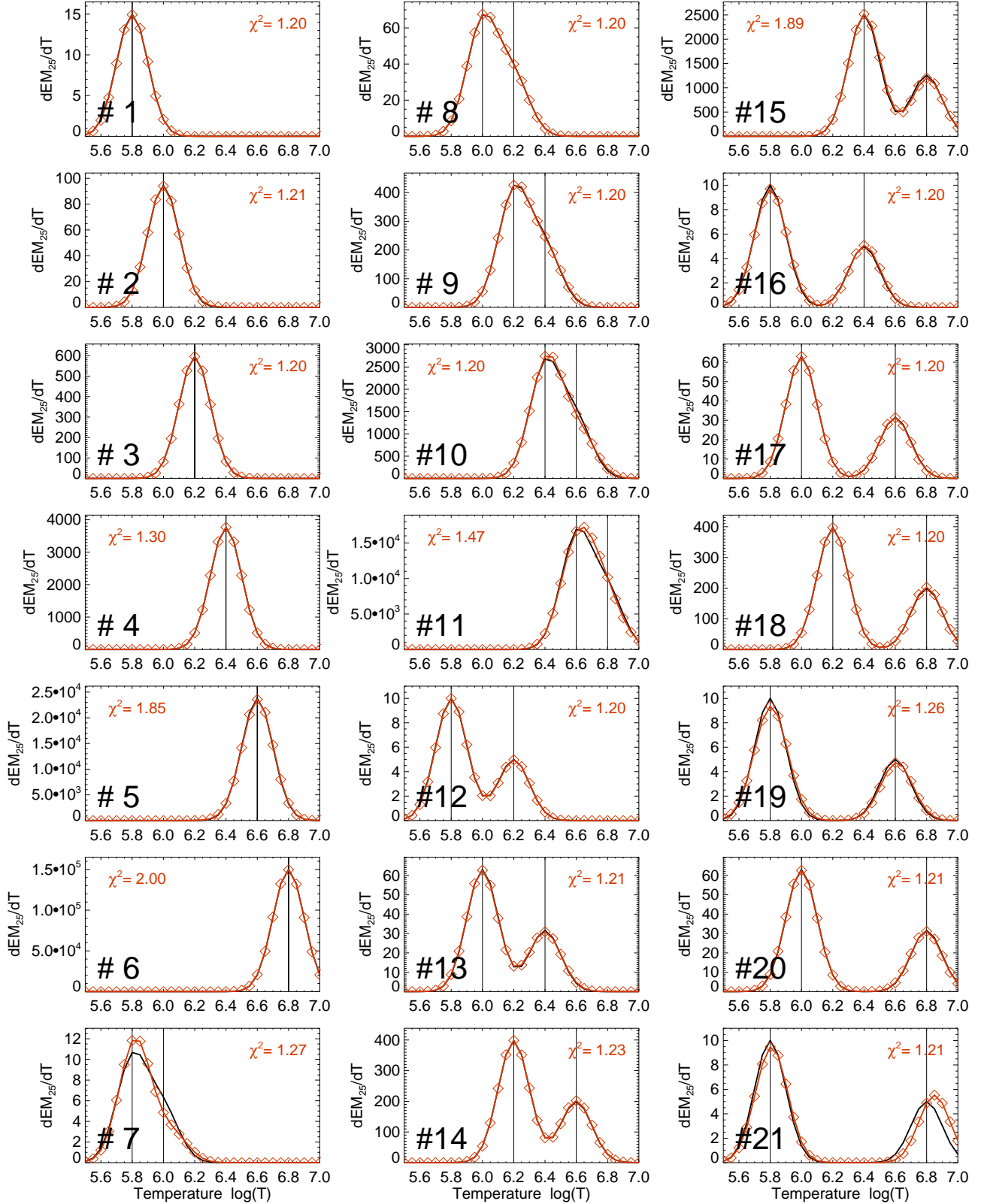


Fig. 11.— A set of 21 simulated DEM distributions with one narrow (#1-#6) or two Gaussian peaks (#7-#21), shown as black curves with the location of the temperature peaks marked with vertical lines. These DEMs have been convolved with the instrumental response functions of the 6 AIA filters for $n_w = 20$ pixels of a Gaussian loop cross-section, with photon noise added, and inverted with forward-fitting of a double-Gaussian DEM model (red curves and diamonds). The χ^2 -squares indicate the goodness of the best fit (see